

# Shortwave infrared detection of medical radioisotope Cerenkov luminescence

Jan Grimm (✉ [grimmj@mskcc.org](mailto:grimmj@mskcc.org))

Memorial Sloan Kettering Cancer Center <https://orcid.org/0000-0002-5282-9385>

**Benedict Mc Lamey**

Memorial Sloan Kettering Cancer Center

**Qize Zhang**

Memorial Sloan Kettering Cancer Center

**Edwin Pratt**

Memorial Sloan Kettering Cancer Center

**Magdalena Skubal**

Memorial Sloan Kettering Cancer Center

**Elizabeth Isaac**

Memorial Sloan Kettering Cancer Center

**Hsiao-Ting Hsu**

Memorial Sloan Kettering Cancer Center

**Anuja Ogirala**

Memorial Sloan Kettering Cancer Center

---

## Article

### Keywords:

**Posted Date:** February 2nd, 2022

**DOI:** <https://doi.org/10.21203/rs.3.rs-1321954/v1>

**License:**  This work is licensed under a Creative Commons Attribution 4.0 International License.

[Read Full License](#)

---

# Shortwave infrared detection of medical radioisotope Cerenkov luminescence

Benedict E. Mc Larney<sup>1,2</sup>, Qize Zhang<sup>1,2</sup>, Edwin C. Pratt<sup>1,2</sup>, Magdalena Skubal<sup>1,2</sup>, Elizabeth Isaac<sup>1,2</sup>, Hsiao-Ting Hsu<sup>1,2</sup>, Anuja Ogirala<sup>1,2</sup>, Jan Grimm<sup>1,2,3,4,5,\*</sup>

1. Molecular Pharmacology Program, Memorial Sloan Kettering Cancer Center, New York, NY, USA
  2. Molecular Imaging Therapy Service, Memorial Sloan Kettering Cancer Center, New York, NY, USA
  3. Pharmacology Program, Weill Cornell Medical College, New York, NY USA
  4. Department of Radiology, Memorial Sloan Kettering Cancer Center, New York, NY, USA
  5. Department of Radiology, Weill, Cornell Medical Center, New York, NY, USA
- \* . Corresponding author: Jan Grimm - [grimmj@mskcc.org](mailto:grimmj@mskcc.org)

## Abstract

Cerenkov luminescence (CL) is produced by medical radioisotopes when charged (commonly beta ( $\beta^{+/-}$ )) particles travel faster than light in a dielectric medium (tissue). This blue-weighted luminescence is both continuous and proportional to the reciprocal wavelength. CL imaging (CLI) promises an economical alternative to PET but is limited by the optical properties of tissue and special setup requirements. CL has been detected in the shortwave infrared (SWIR) spectrum (900 – 1700 nm) from linear accelerators operating in the MeV range but so far not from medical radioisotopes. This work is the first to show that the order of magnitude weaker SWIR CL from medical radioisotopes predicted by the Frank-Tamm equation can also be detected, using commercially available SWIR components. SWIR CL was detected from five clinical radioisotopes: <sup>90</sup>Y, <sup>68</sup>Ga, <sup>18</sup>F, <sup>89</sup>Zr, <sup>131</sup>I and from <sup>32</sup>P, used in biomedical research. The advantage of radioisotope SWIR CLI over conventional CLI is shown in terms of significantly increased light penetration and reduced scattering at tissue depth, in line with the known advantages of SWIR imaging. We report the radioisotope SWIR spectrum, the current detection sensitivity limit (0.23  $\mu$ Ci/ $\mu$ l of <sup>68</sup>Ga) and determine the feasibility of SWIR CLI with *ex vivo* and *in vivo* preclinical examples. Further improvements in SWIR optics and technology are required to enable widespread adoption.

## 1. Introduction

CL is generated by subatomic suprelativistic particles (i.e., traveling faster than the speed of light) in a dielectric medium such as water or tissue.[1] As the particle travels it polarizes the surrounding molecules, which generate light (luminescence) upon relaxation [2]. CL is UV weighted, appearing blue, with an exponential decrease in photon production as the wavelength increases ( $1/\lambda^2$ ) throughout the visible and into the infrared spectrum.[3] The detected CL intensity is directly correlated to the energy of the emitted particle upon decay of the isotope and has found a variety of uses in astrophysics, nuclear physics, and more recently in biomedic imaging.[4, 5]

Cerenkov luminescence imaging (CLI) has been established as a cost- and time-effective alternative to positron emission tomography (PET), especially for surface-weighted imaging.[2, 6] Biomedical CLI has focused on two different entities: the detection of CL from radioisotopes decaying with a beta ( $\beta^{+/-}$ ) particle emission used in nuclear medicine; and from a linear accelerator (LINAC) in the pre- and clinical domain.[7, 8] The advantages of using inexpensive (in comparison to PET) optical based systems to detect signals from specific radiotracers has aided in the discovery and development of both novel targeted radiotracers and radiotherapy-

51 based treatments.[9] The success of preclinical CLI has led to the implementation of clinical CLI.  
52 To date, clinical CLI has focused on image guided surgery for margin detection, determining the  
53 clinical uptake of radiotracers and real time dosimetry readings.[10-13] Numerous clinically  
54 approved and commonplace radioisotopes have been shown to produce detectable CL with  
55 standard administered doses.[4]

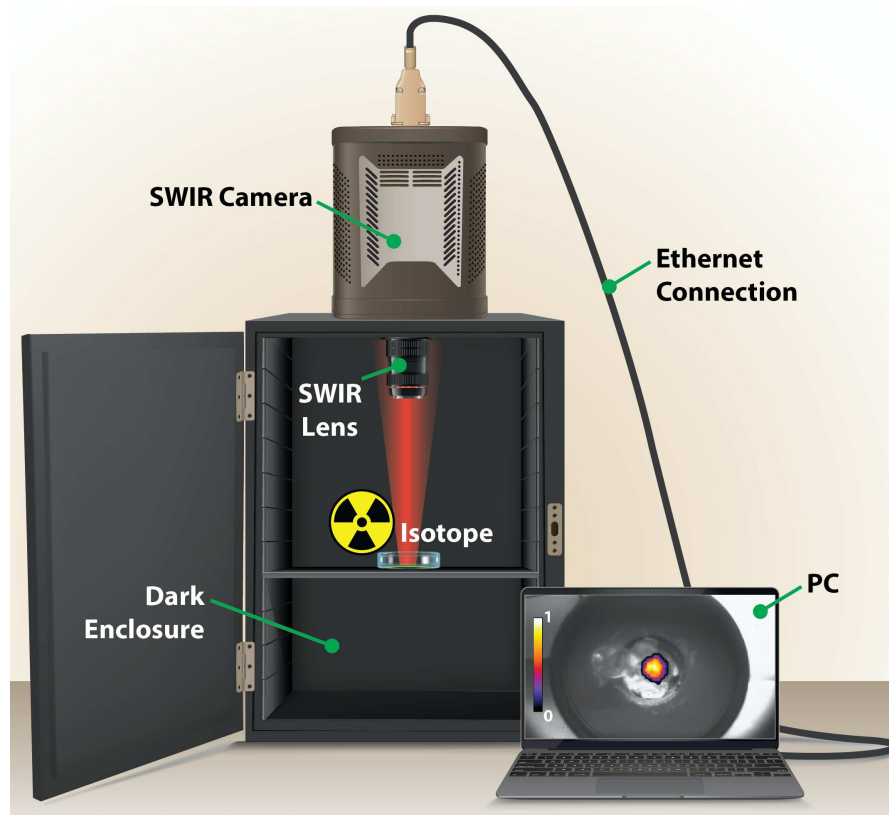
56  
57 The rapid adoption of devices capable of detecting single photons of light by the life science  
58 community has resulted in a wide selection of affordable and low dark and read noise optical  
59 devices. Fortunately these cameras, based on EMCCD and scientific CMOS technology, are  
60 highly sensitive to the blue weighted CL spectrum.[2] Whilst visible wavelengths of light are often  
61 desirable in both fluorescence and microscopy-based imaging, these wavelengths suffer  
62 significant drawbacks in both the pre- and clinical settings. The abundance of endogenous  
63 chromophores in biological tissue limits the optical detection of CL in the visible parts of the  
64 spectrum to penetration depths of a few millimeters.[14] Furthermore, light only remains within its  
65 ballistic regime for a few hundred microns in tissue before entering the scattering or random walk  
66 regime.[15] This greatly reduces the resolution, contrast and ultimate sensitivity of visible light  
67 imaging at increased depth. Accordingly, CLI is limited by the same optical properties of tissue.

68  
69 As the limitations of visible light (VIS)-based imaging have been defined, there has more recently  
70 been a noted shift to longer wavelength-based imaging where the absorption and scattering of  
71 light is reduced.[16] These methods have focused on imaging in the near infrared region (NIR)  
72 above 650 nm where tissue absorption is reduced by almost two orders of magnitude compared  
73 to visible wavelengths (400 – 650 nm).[14, 17] Accordingly, numerous studies have focused on  
74 the red shifting conversion of CL via dyes and nanoparticles.[18-20] Of note is the more recent  
75 emergence of short-wave infrared (SWIR; 900 – 1700 nm) based imaging where tissue  
76 absorption, scattering and autofluorescence are of negligible levels.[21] The advantages of SWIR  
77 imaging have been outlined in many cases including the imaging of the clinically approved dye  
78 ICG with increased resolution and contrast over VIS and NIR wavelengths.[22] Recent examples  
79 have shown the detection of SWIR photons from nanoprobe excited by X-ray beams and  
80 fluorescent emission of quantum dots excited by CL from an external LINAC beam in a FRET  
81 manner.[18, 23-25] Furthermore, pure CLI without the need for secondary emitters has been  
82 detected from LINAC sources where significant improvements were shown by SWIR CL versus  
83 VIS-NIR CL.[26] In comparison to LINAC based CLI, imaging of medical radioisotopes CL is more  
84 demanding. On average, radioisotopes produce an order of magnitude less energy than LINAC  
85 particles achieve (6 to 24 MeV from LINACs versus 0.836 MeV for e.g.  $^{68}\text{Ga}$ , one of the brightest  
86 CL medical radioisotopes).[27-30] The low CL production from radioisotopes requires complete  
87 darkness during imaging in combination with low noise and highly efficient optical imaging  
88 systems. The low luminescence production of radioisotopes in comparison to LINACs additionally  
89 increases the difficulty for radioisotope SWIR CL detection.[3] Furthermore, the acquisition of CL  
90 generated by a LINAC can be synchronized with the radiation pulses for better sensitivity,  
91 something not possible for radioisotope decay.[28, 31] Despite these challenges, we show here  
92 for the first time that SWIR CLI can be performed with medical radioisotopes with significant  
93 advantages over VIS CLI.

94  
95 Currently, commercial SWIR technology is far less advanced than its visible light EMCCD  
96 counterparts in terms of both sensor read and dark charge noise. Thermoelectric cooled (TEC)  
97 EMCCDs can readily achieve dark noise levels of 0.001 e/p/s in comparison to values ranging  
98 from 40 to 300 e/p/s for TEC cooled SWIR sensors. Additionally, high efficiency visible light  
99 collecting optics are commercially available with an  $f$  of 0.95. This is in stark comparison to  
100 commercially available SWIR lenses which currently achieve an  $f$  of only 1.4, collecting less than  
101 half the light of 0.95 lenses. The low light output of radioisotope CL, orders of magnitude increased

102 SWIR dark and read sensor noise in combination with less sensitive lenses further exacerbates  
103 the challenge to detect radioisotope SWIR CL. In this work, radioisotope SWIR CLI was achieved  
104 via specialized TEC SWIR cameras, appropriate acquisition settings and post acquisition  
105 processing. Herein we characterize the performance of SWIR CL with radioisotopes, detect SWIR  
106 CL emission from six radioisotopes, define the SWIR CL radioisotope emission spectrum, show  
107 the advantage of SWIR CLI over VIS CLI, define the current limit of detection in terms of sensitivity  
108 and assess the feasibility of preclinical radioisotope SWIR CL in both *ex vivo* and *in vivo* settings.  
109 This work establishes a proof of principle for radioisotope SWIR CLI. We also highlight the need  
110 for improved SWIR sensors and optics to mature SWIR CLI technology to a level seen with VIS  
111 CLI.

## 112 2. Results



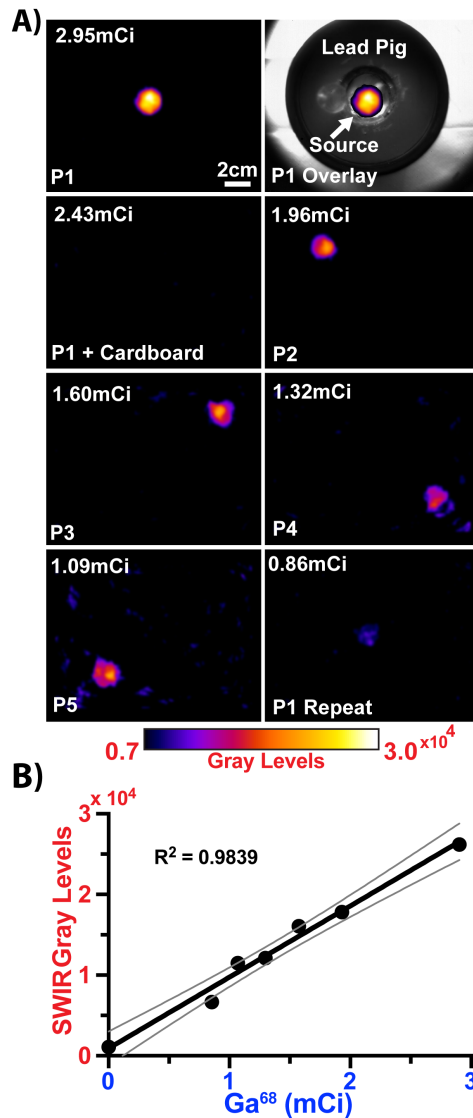
115  
116  
117 **Figure 1. Schematic outlining the SWIR CL radioisotope imaging setup.** Imaging was carried out  
118 in a custom dark enclosure with the radioisotope source located within a lead ingot (pig) for shielding.  
119 The camera was fitted with either a 16mm or 8mm f/1.4 SWIR lens and located 20 cm from the source  
120 with a field of view of 15x15 cm. Camera control and recordings were managed from the respective  
121 camera software on a PC.

### 122 2.1 Confirmation of SWIR CL detection from radioisotopes

124  
125  
126  $^{68}\text{Ga}$  is a commonly administered medical radioisotope for PET imaging.[32, 33] During its decay,  
127  $^{68}\text{Ga}$  produces  $\beta^+$  particles (87.7%) along with  $\gamma$  photons. As shown in Figure 2A, the SWIR CLI  
128 setup (see Figure 1A) could readily detect the SWIR radioisotope CL emission. A sample of  $^{68}\text{Ga}$   
129 (2.95 mCi) was eluted into a 5 ml Eppendorf and placed in a lead pig within the field of view (FOV).

130 Shown in Figure 2A top right is the processed SWIR CL image overlaid on the white light image  
 131 demonstrating that the source of light is coming from the Eppendorf and that the processing steps  
 132 sufficiently removed  $\gamma$  strikes on the camera chip whilst retaining the intensity of the light source.  
 133 To ensure that the image processing did not accumulate  $\gamma$  strikes to resemble the light source, a  
 134 piece of black cardboard was placed over the source. As shown in Figure 2A, the cardboard  
 135 image resulted in a blank image confirming that the images are based on the the detection of  
 136 SWIR CL photons and not  $\gamma$  strike accumulation. The  $^{68}\text{Ga}$  source was then moved around the  
 137 FOV decaying in the process (five positions in total including a repeat of P1). The sensor could  
 138 readily detect CL from  $^{68}\text{Ga}$  across the entire FOV. Manually drawn regions of interest (ROI)  
 139 were then measured to determine the signal intensity (gray values) of the sensor for each position and  
 140 timepoint.

141



142

143

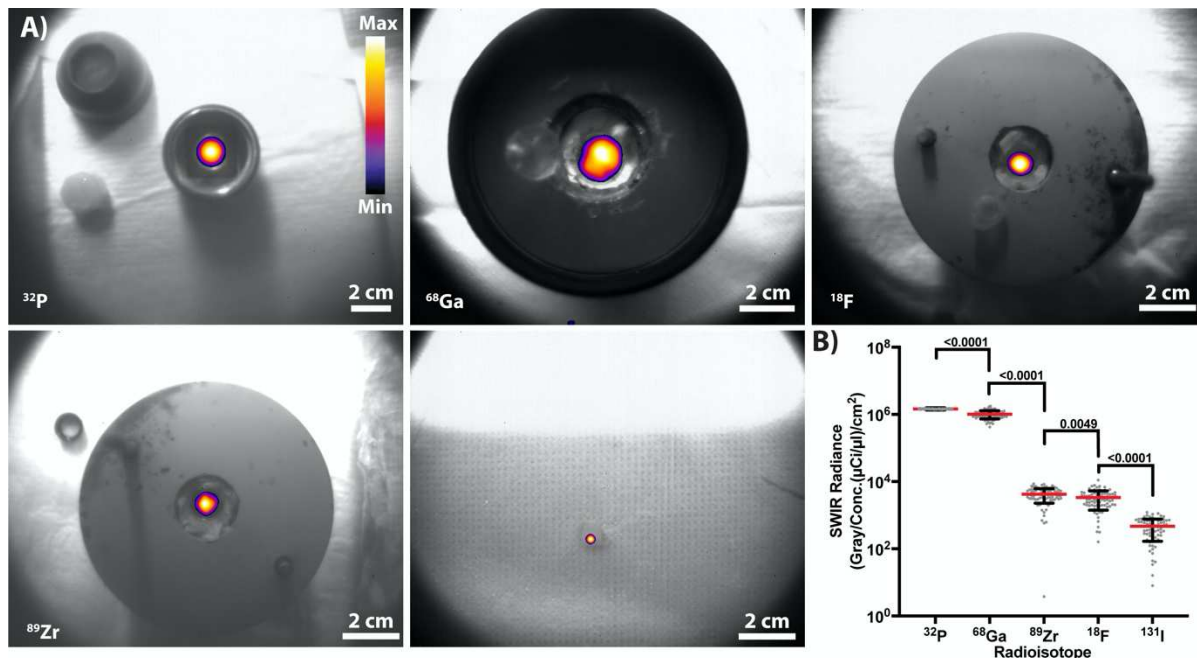
144 **Figure 2. Linearity of the SWIR CLI setup to  $^{68}\text{Ga}$  decay across the FOV.** A) Linearity assessment  
 145 of the camera ensuring images were not processing artifacts. Shown is  $^{68}\text{Ga}$  imaged at positions  
 146 across the FOV. The P1 + Cardboard confirms the detection is not due to  $\gamma$  strikes which can pass  
 147 through the cardboard whilst light cannot. B) The recorded SWIR gray levels and corresponding  $^{68}\text{Ga}$   
 148 activity (mCi) across all positions. The linear regression is shown along with the 95% confidence

149 intervals. The Pearson correlation value is displayed ( $R^2 = 0.9839$ ), two-tailed  $p$  value  $<0.0001$   
 150 highlighting the conserved quantitative and linear response capabilities of SWIR CLI, in line with VIS  
 151 CLI. Each image and data point are a summation of  $n = 90$  technical replicates for each position.  
 152 Presented images are thresholded at the same levels to show lowest light levels, allowing noise and  
 153 sensor artifacts to show at 1.32 and 1.09 mCi.

154  
 155 As can be seen in Figure 2B the recorded gray levels increase in a manner that is linearly  
 156 correlated with the  $^{68}\text{Ga}$  mCi levels highlighting the accuracy and quantitative capabilities of SWIR  
 157 CLI setup at high radioisotope levels. This linearity is in line with VIS CLI.[4] As is common with  
 158 optical imaging devices, linearity and sensitivity are reduced along imaging borders as shown by  
 159 the artefacts at P4 and P5 in Figure 2.

160  
 161 As SWIR CLI could be performed with  $^{68}\text{Ga}$  ( $0.84 \mu\text{Ci}/\mu\text{l}$ ), we set out to investigate other  
 162 radioisotopes which may produce enough SWIR CL to be detected using our setup. As shown in  
 163 Figure 3A, four additional radioisotopes were detected:  $^{32}\text{P}$  ( $8.65 \mu\text{Ci}/\mu\text{l}$ ),  $^{18}\text{F}$  ( $272.25 \mu\text{Ci}/\mu\text{l}$ ),  $^{89}\text{Zr}$   
 164 ( $160 \mu\text{Ci}/\mu\text{l}$ ) and  $^{131}\text{I}$  ( $1112 \mu\text{Ci}/\mu\text{l}$ ). The same processing steps as used for the  $^{68}\text{Ga}$  imaging were  
 165 employed to ensure that the detected signals were not as a result of  $\gamma$  strikes and correctly  
 166 overlaid with the white light image of the source location. In all cases the CL was correctly overlaid  
 167 with the position of the source, see Figure 3A. The SWIR radiance of each was then calculated  
 168 as shown in Figure 3B, values have been corrected for both concentration ( $\mu\text{Ci}/\mu\text{l}$ ) and spatial  
 169 FOV ( $\text{cm}^2$ ). SWIR CLI could readily differentiate between each of the tested radioisotopes, as  
 170 shown by the  $p$  values in Figure 3B. The reported SWIR CL levels are in line with previously  
 171 reported VIS CLI values highlighting the continuity of the technique.[34]

172



173  
 174 **Figure 3. SWIR CLI of a variety of medical radioisotopes.** A) Top and bottom, representative  
 175 images are shown for SWIR CLI detection of  $^{32}\text{P}$ ,  $^{68}\text{Ga}$ ,  $^{18}\text{F}$ ,  $^{89}\text{Zr}$  and  $^{131}\text{I}$ . Each image is thresholded  
 176 respectively and represents the summation of  $n = 90$  technical replicates. B) Comparative descending  
 177 radiance of the isotopes which have been corrected for concentration ( $\mu\text{Ci}/\mu\text{l}$ ) and spatial FOV.  
 178 Student's  $t$ -test (upaired, two-sided)  $p$  values are shown highlighting the systems capability to  
 179 distinguish between radioisotopes. The mean (red line) and standard deviation are shown. Individual  
 180 measurements ( $n = 90$  technical replicates) are displayed with gray dots for each sample, excluding  
 181 negative values.

## 2.2 Determining the SWIR CLI radioisotope temporal detection limit and emission spectrum

$^{32}\text{P}$  is a pure  $\beta^-$  particle emitter with a long half-life of 14.3 days and provides a stable source for setup characterization. The  $^{32}\text{P}$  concentrations used here ensured SWIR CLI detection with signal being distinguished from noise at acquisitions speeds as low as 0.25s, see Figure 4A. Each image panel of Figure 4A represents the summation of 90 frames at each respective exposure time. Figure 4B shows the mean gray level along with each of the 90 repetitions at the respective acquisition length.

The high SWIR CL radiance of  $^{32}\text{P}$  was then used to characterize the radioisotope SWIR CL emission spectrum. No filter (wavelengths of 920nm and above due to the spectral response of the sensor) and long pass filtered acquisitions ranging from 1000 nm to 1500 nm in 100 nm steps were carried out. The sensor used in these experiments employs an indium phosphide (InP) substrate band gap at 1.35 eV. Whilst InGaAs itself can detect VIS light, the InP band gap is not thinned on this device and thus prevents light below 920 nm from reaching the sensor. Additionally, InGaAs focal plane arrays have an inherent bandgap of 0.75 eV resulting in a shortpass cutoff at 1700nm.[35-37] The images of the SWIR CL photon production are shown in Figure 4C with the intensity exponentially decreasing as the wavelength increased, as expected and previously reported for VIS CLI and LINAC based SWIR CLI.[2, 26] The radioisotope SWIR CL spectrum was then quantified as shown in Figure 4D showing a fitted one phase exponential decay with an  $R^2$  of 0.9812. As can be seen in Figure 4C and D detection of photons above 1400nm is challenging with the current setup which can likely be attributed to the noise within the system as opposed to purely low luminescence production. The noise is highlighted by the noise floor level shown in Figure 4D.

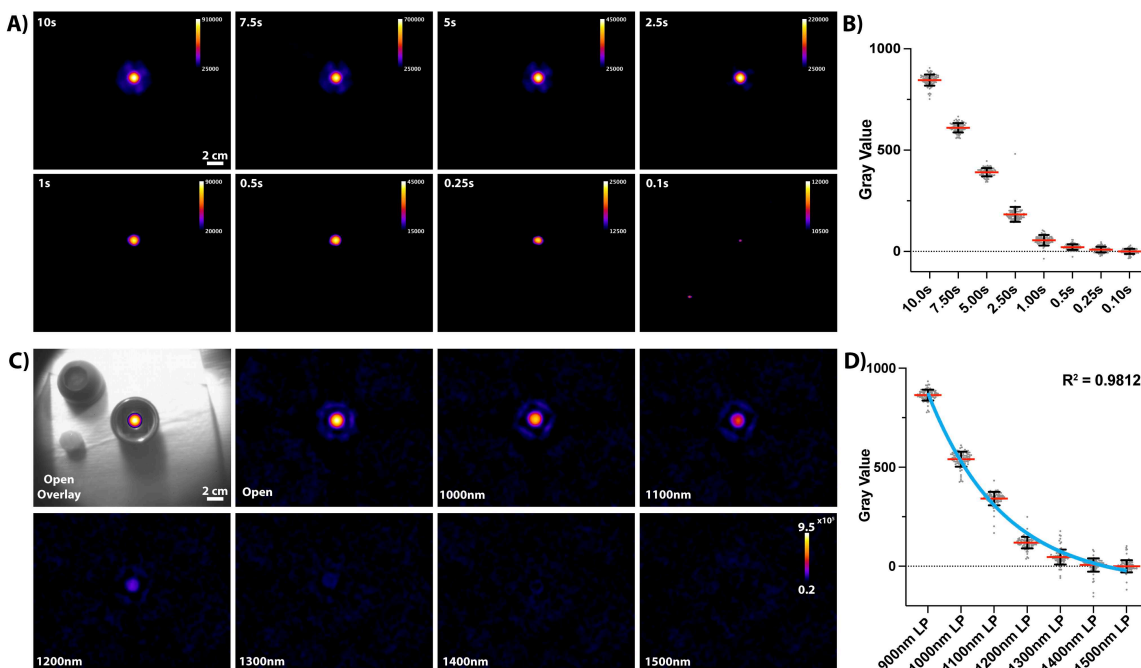
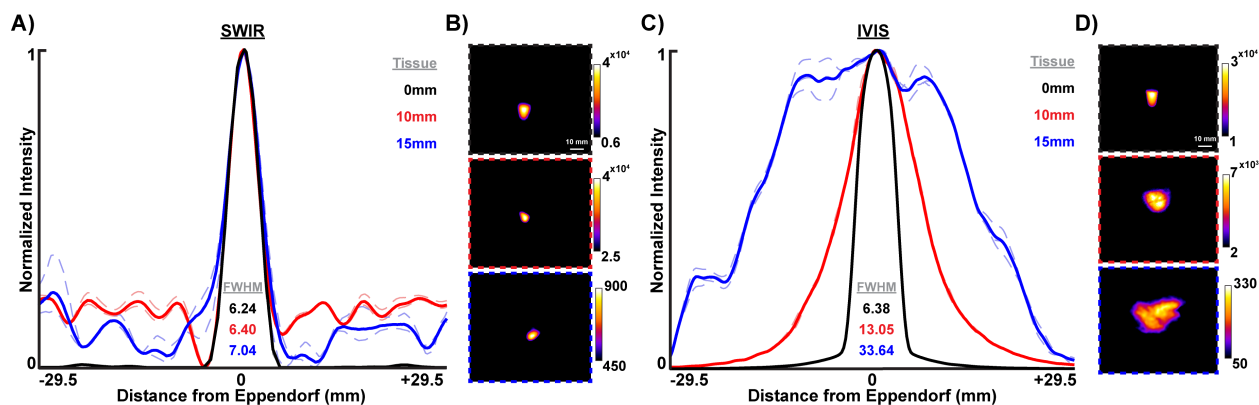


**Figure 4. Determining the radioisotope SWIR CLI temporal acquisition limit and spectrum** A) Representative images of the effect of exposure time changes on image quality for each exposure length. SWIR CL could be separated from the noise at acquisition speeds of up to 0.25s. B) The gray

214 value intensity as exposure time changes. For A) each image is a summation of  $n = 90$  technical  
 215 replicates and B) is representative of each replicate where the mean and standard deviation are  
 216 displayed. C) The SWIR CL emission spectrum of  $^{32}\text{P}$  is shown. Firstly, overlaid and then by images  
 217 for each filter set. The output decreases as the wavelength increases. Each image is a summation of  
 218  $n = 90$  technical replicates. D) Graphical representation of the radioisotope SWIR CL emission  
 219 spectrum from 920 to 1500 nm, mean and standard deviation are displayed from  $n = 90$  technical  
 220 replicates. A one phase exponential decay function has been fitted ( $R^2 = 0.9812$ ). As shown in C) the  
 221 inherent noise in the system and low photon production prevents detection of photons above 1400  
 222 nm.

### 224 2.3 Reduced scattering via SWIR CLI over VIS CLI

226 Having established suitable acquisition and post processing steps, we then investigated the  
 227 advantage of SWIR over VIS CLI. To achieve this an eppendorf containing 1.5 mCi of  $^{90}\text{Y}$   
 228 suspended in 200  $\mu\text{l}$  of saline solution was imaged on the SWIR setup and immediately after on  
 229 a current state of the art IVIS<sup>®</sup> (VIS CLI) imaging system.  $^{90}\text{Y}$  is a pure  $\beta^-$  emitter (only CL) with a  
 230 64h half life that is commonly administered clinically to treat primary and metastatic liver cancer  
 231 at activities ranging from 13.5 to 143 mCi.[38, 39] Representative images of the source with and  
 232 without overlying scattering medium (chicken breast) were acquired on the SWIR and IVIS  
 233 systems at increasing tissue depths of 0, 10 and 15 mm. To enable a fair comparison between  
 234 both modalities the imaging time was defined as the minimum time needed to detect signal from  
 235 the source without any scattering medium, 10 s for IVIS imaging and 15 mins for SWIR CLI. These  
 236 exposure times were consistent throughout the increase in tissue depth. As can be seen in Figure  
 237 5, SWIR CLI shows an improvement in resolution when imaging through scattering tissue.  
 238 Observationally, for SWIR CLI the shape of the Eppendorf containing  $^{90}\text{Y}$  remains consistent up  
 239 to 15 mm of tissue whilst its appearance is enlarged over five times in VIS CLI. This highlights  
 240 the advantage of SWIR CLI over VIS CLI to accurately resolve radioisotope's location at depth in  
 241 scattering media like tissue. This accuracy is further validated by the full width half maximum  
 242 (FWHM) measurements shown in Figures 5 A and C.

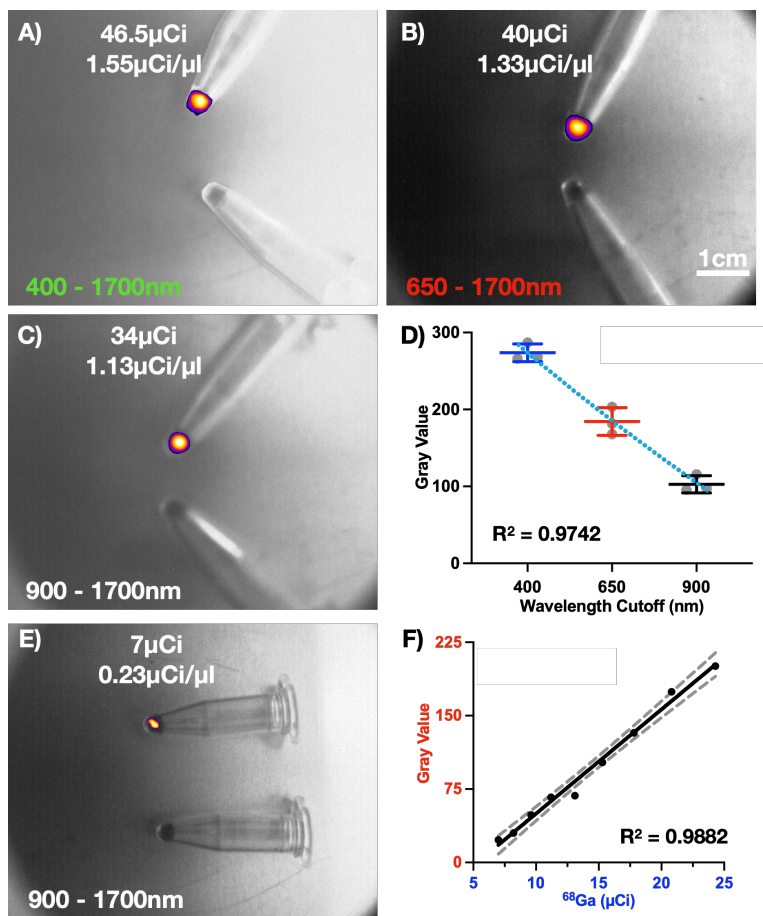


244  
 245  
 246 **Figure 5. SWIR CLI enables reduced scattering in tissue over VIS CLI** A) Normalized SWIR  
 247 CLI intensity profiles of an eppendorf containing 1.5 mCi of  $^{90}\text{Y}$  suspended in 200  $\mu\text{l}$  of saline  
 248 solution with increasing depths of scattering tissue (chicken breast at depths of 0, 10 and 15 mm)  
 249 with respective full width half maximums (FWHM) of 6.24, 6.40 & 7.04 mm. B) Representative  
 250 SWIR CL images of the eppendorf through increasing scattering tissue depths. C) Normalized  
 251 VIS CLI intensity profiles of VIS CLI line profiles (IVIS) from the phantom setup used in A). FWHMs  
 252 increase with scattering tissue depth at 0, 10 and 15 mm with respective FWHMs of 6.38,  
 253 and 33.64 mm. D) Representative VIS CLI images of the source as seen through scattering tissue

254 depths. In all cases three separate line measurements are made from the images at each depth  
255 (dotted lines) with the mean shown by the solid line.

## 257 2.4 SWIR CLI radioisotope sensitivity limits *in vitro*

258  
259 As previously mentioned, the majority of SWIR sensors are insensitive to wavelengths of light  
260 below 920nm. However, by thinning the InP cap, the low cutoff can be improved to ~400 nm with  
261 the sensor then capable of detecting VIS and SWIR wavelengths. Whilst the camera has a largely  
262 increased range, it is still very insensitive in comparison to e.g. EMCCDs. It should be noted that  
263 the VIS sensitivity of a second sensor (Zephyr 1.7v, Photon Etc., Canada) used in this study has  
264 significantly reduced quantum efficiency in the VIS range (e.g. ~25% at 600 nm). The sensor was  
265 employed to compare the spatial localization of VIS-SWIR (400 – 1700 nm), NIR-SWIR (650 –  
266 1700 nm) and SWIR CLI (900 – 1700 nm) of radioisotopes via appropriate long pass optical filters.  
267 Silica nanoparticles (SiNPs) have been shown to readily bind radioisotopes with a high affinity  
268 and are suitable for localized injection *in vivo* preventing unwanted distribution of the  
269 radioisotope.[40] In Figure 6, <sup>68</sup>Ga conjugated SiNPs suspended in 30  $\mu$ l of saline opposite a non-  
270 radiolabeled SiNP control were imaged at VIS-SWIR, NIR-SWIR, and again at SWIR following  
271 numerous half-lives. As can be seen in Figure 6 A) – C), the spatial location of the detected CL  
272 signals through the defined spectrums are solely localized to the eppendorf containing <sup>68</sup>Ga +  
273 SiNPs. The overall activity along with the activity per  $\mu$ l are shown. In Figure 6 D) the sensitivity  
274 of SWIR CLI is shown with a detection limit of 7  $\mu$ Ci (0.23  $\mu$ Ci/ $\mu$ l) for <sup>68</sup>Ga labelled SiNPs.  
275

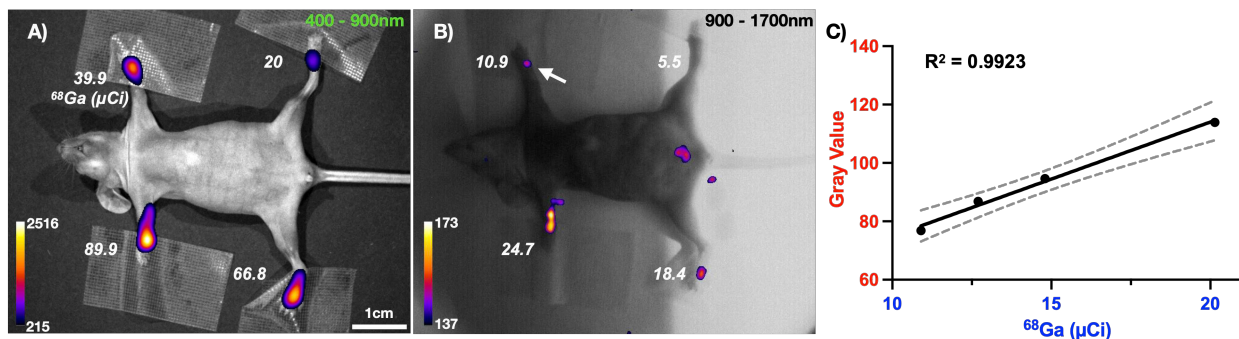


276  
277

278 **Figure 6. SWIR CLI radioisotope sensitivity limits for  $^{68}\text{Ga}$  labeled SiNPs.** **A)** VIS to SWIR  
 279 (400 - 1700 nm) image of  $^{68}\text{Ga}$  radiolabeled SiNPs (Top) and non-radiolabeled SiNPs (Bottom).  
 280 **B)** NIR to SWIR (650 – 1700 nm) image of the same phantom as in A). **C)** SWIR image of the  
 281 same phantom as in A). **D)** Decay corrected emission profile quantification of the labeled  $^{68}\text{Ga}$   
 282 SiNPs,  $n = 3$  technical replicates, median and standard deviation are shown. The dotted line  
 283 represents a fitted one phase exponential decay with the goodness of fit shown ( $R^2 = 0.9742$ ). **E)**  
 284 The SWIR CLI radioisotope sensitivity limit for  $^{68}\text{Ga}$  labeled SiNPs post multiple half-lives. **F)**  
 285 Tracking the decay for the SWIR CLI limit of detection (900nm LP Filter). The linear regression is  
 286 shown with 95% confidence intervals with a goodness of fit  $R^2 = 0.9882$ , highlighting that at these  
 287 low levels SWIR CLI performs linearly in relation to radioisotope levels.  
 288

## 2.5 SWIR CLI radioisotope sensitivity limits ex vivo

291 Having determined the *in silico* detection limits of SWIR CLI to be 7  $\mu\text{Ci}$  (0.23  $\mu\text{Ci}/\mu\text{l}$ ) for  $^{68}\text{Ga}$  for  
 292 radiolabeled SiNPs, we then tested the detection limits in tissue. A nude mouse was euthanized  
 293 via  $\text{CO}_2$  inhalation and injected with 30  $\mu\text{l}$  of  $^{68}\text{Ga}$  labelled SiNPs into each respective paw with  
 294 varying radioisotope activities. Confirmation of the SiNPs location can be seen in Figure 7 A  
 295 acquired with the IVIS system (VIS CLI). The same mouse was then transferred to the same  
 296 SWIR CLI system as used in Figure 6 and imaged post multiple half-lives to determine the *post*  
 297 *vivo* sensitivity SWIR CLI sensitivity (900 nm LP filter). As can be seen in Figure 7B,  $^{68}\text{Ga}$  labeled  
 298 SiNPs were successfully detected down to 10.9  $\mu\text{Ci}$ , far below activity levels administered  
 299 clinically (typically 4000  $\mu\text{Ci}$ ).[41]  
 300

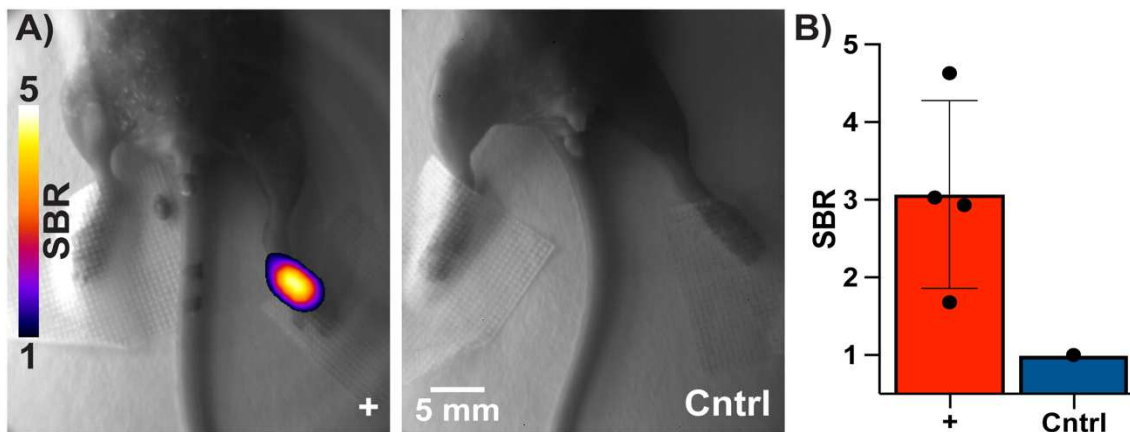


301 **Figure 7. Ex vivo SWIR CLI radioisotope sensitivity limits** **A)** VIS CLI (IVIS - 400 to 900 nm)  
 302 image of 30  $\mu\text{l}$  of  $^{68}\text{Ga}$  labeled SiNPs injected subcutaneously into a dead mouse paw labeled  
 303 with varying amounts of  $^{68}\text{Ga}$ .  $^{68}\text{Ga}$  amounts are shown in white text in  $\mu\text{Ci}$ . **B)** The ex vivo SWIR  
 304 CLI (900 – 1700 nm) limit of detection for  $^{68}\text{Ga}$  labeled SiNPs in the same mouse as in A) post  
 305 multiple half-lives. As expected, the detection limit worsens in tissue compared to *in silico* imaging  
 306 (~3  $\mu\text{Ci}$  less sensitive). **C)** Linear regression analysis of the ex vivo SWIR CLI of the  $^{68}\text{Ga}$  labeled  
 307 SiNPs to the limit of detection (10.9 $\mu\text{Ci}$ , B) paw labeled with the white arrow). SWIR CLI detection  
 308 in tissue behaves linearly in relation to  $\mu\text{Ci}$  amounts ( $R^2 = 0.9923$ ).  
 309  
 310  
 311

## 2.6 In vivo detection of radioisotope SWIR CLI

312 Whilst  $^{68}\text{Ga}$  produces bright CL, the combination of it's short half-life (68 mins), the increased  
 313 noise of current SWIR CLI system and increased  $\gamma$  strikes rendered  $^{68}\text{Ga}$  unsuitable for longer  
 314 term experiments. To counteract the short comings of both  $^{68}\text{Ga}$  and SWIR imaging we employed  
 315  $^{90}\text{Y}$  (average  $\beta$  energy of 0.94 MeV, 64.1 hour half-life) conjugated to SiNPs for *in vivo* SWIR CLI  
 316 radioisotope detection.[40] Additionally,  $^{90}\text{Y}$  has been shown to improve the SNR of CL detection  
 317  
 318

319 as the produced  $\beta^-$  do not result in 511 keV photon production as is found with  $\beta^+$  sources e.g.  $^{18}\text{F}$   
 320 or  $^{68}\text{Ga}$ . [42] The long exposure times for SWIR CLI enabled contamination of the SWIR CL image  
 321 with a thermal signature, further complicating SWIR CLI in comparison to VIS CLI. Mice which  
 322 had been injected with  $\sim 200 \mu\text{Ci}$  of  $^{90}\text{Y}$  labeled SiNPs were imaged 3 hours post injection into a  
 323 single footpad.  $^{90}\text{Y}$  is administered clinically for radioembolization at activities ranging from 13,500  
 324 to 143,000  $\mu\text{Ci}$ . [38, 39] As can be seen in Figure 8 and Supplemental Figure 3 the SWIR CLI  
 325 signal was readily detected over background thermal signatures present *in vivo* ( $n = 4$  mice).  
 326 Radiolabeled SiNPs injected in the foot slowly migrate through the lymphatic system (on the order  
 327 of 48 hrs) preventing CL contamination of the inherent thermal signature. [40] To highlight the  
 328 SWIR CL signal, the respective thermal signature from each mouse was used to divide the image  
 329 producing measurements in terms of signal to thermal background ratio (SBR). The performed  
 330 image processing steps can be seen in Supplemental Figure 1. This processing method  
 331 suppressed the inherent thermal signal in the control mouse, shown in Figure 8. As can be seen  
 332 in Figure 8 B, SBRs from injected mice ranged from 1.68 to 4.63 with a mean of 3.07.  
 333



334  
 335  
 336 **Figure 8. In vivo SWIR CLI detection of  $^{90}\text{Y}$  labeled SiNPs three hours post injection into**  
 337 **the footpad A) Left, Representative images of a mouse injected (+) with  $^{90}\text{Y}$  labeled SiNPs ( $\sim 200$**   
 338  **$\mu\text{Ci}$ ).** Right, image of a control mouse without any injection. **C) Quantified SBR values of injected**  
 339 **( $n = 4$ ) vs control mice ( $n = 1$ ).** All images are shown in respective signal to background ratios  
 340 (SBR).  
 341

### 342 3. Discussion

343  
 344 This work set out to prove that SWIR CLI could be detected from radioisotopes from  
 345 commercially available SWIR technology. Previous work has shown SWIR CL produced by  
 346 accelerated beams from LINAC sources, which have on average an order or more magnitude  
 347 higher energy levels than  $\beta$  particles from radioisotopes. [23, 26] The employed enclosure  
 348 provided an imaging environment free of ambient room lights as is necessary with radioisotope  
 349 VIS CLI. [43, 44] The TEC SWIR sensors used here, whilst state of the art, produce 2 to 3 orders  
 350 of magnitude higher dark charge noise in comparison to e.g. TEC EMCCD counter parts.  
 351 Despite this, SWIR CLI was detected from a variety of medical radioisotopes, see Figure 3A,  
 352 and the detected SWIR radiance levels are in line with radioisotope production in VIS CLI. [34]  
 353 We have also shown that in line with VIS CLI, SWIR CLI linearly correlated with both high and  
 354 low radioisotope levels in multiple settings, see Figures 2, 6 and 7. We have shown the  
 355 radioisotope sensitivity limit of SWIR CLI to be as low as  $7 \mu\text{Ci}$  ( $0.23 \mu\text{Ci}/\mu\text{l}$ ) *in vitro* and as low  
 356 as  $10.9 \mu\text{Ci}$  in tissue with  $^{68}\text{Ga}$ . This is in stark contrast to VIS CLI performed with EMCCDs  
 357 where  $^{68}\text{Ga}$  detection has been reported as low as  $0.00009 \mu\text{Ci}/\mu\text{l}$ , over four orders of

358 magnitude more sensitive than SWIR CLI.[45] As a result, the insensitivity of SWIR CLI limits  
359 applications in its current iteration. However, the significant advantage of reduced scattering in  
360 SWIR CLI as shown here in Figure 5 could significantly improve radioisotope CLI  
361 applications.[26] Based on these results the advantage of radioisotope SWIR CLI would enable  
362 the better resolution of deep seated tumor radioisotope uptake.[17, 46, 47]  
363

364 The SWIR CLI setup used here was capable of detecting radioisotope emissions at temporal  
365 resolutions of up to 0.25s, verging on the potential for video rate imaging, as shown in Figure 4A.  
366 However,  $^{32}\text{P}$  and the amount of radioisotope used in this case is only suitable for *in silico*  
367 experimentation and enabled this proof of principle investigation. Furthermore,  $^{32}\text{P}$  undergoes  
368 pure  $\beta^-$  decay reducing the impact of  $\gamma$  strikes on the sensor and improving sensitivity.[42] The  
369 long half-life of  $^{32}\text{P}$ , further enabled quantification of the radioisotope SWIR CL spectrum, found  
370 to be in line with the SWIR CL spectrum produced by LINACs.[26] Due to the inherent noise in  
371 SWIR systems, detection of CL could not be reliably determined from noise above 1400 nm. A  
372 more sensitive system with reduced noise, similar to that of EMCCD cameras should be able to  
373 detect these longer wavelengths whilst simultaneously detecting lower radioactivity levels.  
374 However, the advantage of wavelengths above 1400 nm is unclear for SWIR CLI due to the  
375 increased absorption of water in this region.[17, 46]  
376

377 Having performed SWIR CLI from a range of radioisotopes, determined the sensitivity limits and  
378 shown the advantage of radioisotope SWIR CLI over VIS CLI our focus then turned to the  
379 preclinical potential of SWIR CLI. The success of preclinical VIS CLI has been widely established  
380 due to its relative ease and the wide availability of highly sensitive (single photon) cameras.[48-  
381 51] Initial experiments focused on *ex vivo* SWIR CLI to detect  $^{18}\text{F}$ -FDG locally injected to a tumor  
382 on a xenografted mouse (see Supplemental Figure 2). However, the weak CL production of  $^{18}\text{F}$   
383 (22 times dimmer than  $^{68}\text{Ga}$ ) required the intratumoral administering of mCi's of radioisotope and  
384 lengthy acquisition times on the order of an hour for accurate signal detection.[45]  $^{90}\text{Y}$  is a brighter  
385 CL source than  $^{68}\text{Ga}$  with a longer half-life (64.2 hrs versus 1.13 hrs) and overcomes the  
386 limitations of  $^{68}\text{Ga}$  and  $^{18}\text{F}$  for this investigation.[2, 34]  $^{90}\text{Y}$  labeled SiNPs were synthesized as  
387 previously described and injected into the foot of live mice to enable *in vivo* SWIR CLI  
388 detection.[40] Four mice were imaged 3 hours post injection with  $\sim 200$   $\mu\text{Ci}$  of  $^{90}\text{Y}$ -SiNPs,  
389 respectively along with a non-injected control mouse. In this case, an imaging time of 15 mins  
390 provided a reliable signal that could be detected over the endogenous thermal signature, see  
391 Figure 8. This is the first case of radioisotope SWIR CLI *in vivo* detection and proves the potential  
392 for *in vivo* radioisotope SWIR CLI.  
393

394 Throughout the course of these experiments the main limiting factor has been the intrinsic noise  
395 within the SWIR setup, an obstacle not only for SWIR CLI.[52] The orders of magnitude noise  
396 increase compared to EMCCD detectors and reduced light output at these longer wavelengths  
397 requires longer exposure times (tens of minutes versus seconds to minutes). This long exposure  
398 time is a significant disadvantage for SWIR CLI and counteracts one of the benefits of CLI i.e.  
399 short acquisition times. The SWIR sensors used here are not capable of performing on chip  
400 binning and are limited to post processing binning, additionally reducing the sensitivity and  
401 acquisition speed when compared to EMCCDs. Further hampering signal detection is the limited  
402 commercial availability of efficient light collection (fast) SWIR lenses. In this case an  $f/1.4$  was  
403 achieved whilst numerous VIS CLI spectrum lenses collect more than double the light with an  
404  $f/0.95$ . [53-55] To counteract this we utilized lenses with a short focal length (8 or 16 mm) to  
405 decrease the distance to the source, increasing light collection. However, imaging with such short  
406 focal lengths comes at the cost of reducing the effective depth of field, especially in comparison  
407 to the current preclinical gold standard IVIS imaging. Future iterations of SWIR CLI systems  
408 should aim to tackle these two main current limitations with a faster lens and dark noise reduced

409 camera sensor. Such a lens and sensor will be highly custom devices and are outside the scope  
410 of this proof of principle work.

411  
412 Considering that human eyes respond to light from ~400 to ~700 nm it would be feasible to change  
413 the lights used in CLI locations from bulbs which produce SWIR light to non-SWIR emitting LEDs.  
414 The use of such room lighting in combination with SWIR CLI could enable radioisotope CLI to be  
415 carried out in a well lit room and without the need for a dark enclosure, as has been achieved for  
416 LINAC CLI.[28] This may have impact in preclinical small animal imaging where CLI is commonly  
417 used as a cheap alternative to PET for the tracking of novel radiotracers and treatments.[49, 56]  
418 However, significant improvements are required in SWIR optics and technology before this can  
419 be realized.

420

## 421 **4. Methods & Materials**

422

### 423 **4.1 Radioisotope SWIR Setup**

424

425 Detection of SWIR CLI was carried out using thermoelectronically cooled (TEC) InGaAs focal  
426 plane arrays (NIRVana 640 TE, Princeton Teledyne, NJ, USA or ZephIR 1.7x, Photon etc Inc.,  
427 Montreal, Canada) mounted on a custom enclosure as outlined in Figure 1. The custom built  
428 aluminium enclosure has an adjustable stage and lockable door. SWIR CL collection was  
429 achieved via a SWIR lens (SWIR-16, Navitar, NY, USA or 8mm FL SWIR lens, stock #83-815,  
430 Edmund Optics, NJ, USA) mounted on the camera. In all cases the lens aperture was set to an  
431  $f/1.4$  to allow maximum collection of light. Data presented in Figures 2, 3 and 4 were acquired  
432 without the addition of optical filters, the NIRVana 640 TE focal plane array used in these  
433 acquisitions has not had InP cap layer thinning performed, preventing it detecting photons below  
434 920 nm.[57] Data in all other figures was acquired with the addition of either an 650nm or 900 nm  
435 O.D. 4.0 long pass filter (Edmund Optics #84-759 & #84-764, NJ, USA) mounted to the front of  
436 the lens. Acquisition settings along with recording of data was controlled via each cameras  
437 respective acquisition software. Due to the high noise levels associated with InGaAs sensors in  
438 comparison to more developed technology such as EMCCDs, acquisitions were limited to an  
439 accumulation of 90 frames of 10s each (900s/15mins total recording time). This ensured that  
440 Cerenkov light could be detected over the fundamental noise in the system. Dark noise  
441 measurements were recorded for each sensor and subtracted from the SWIR CL signal. White  
442 light (WL) images were taken with the enclosure door open and room lights on.

443

### 444 **4.2 Determining SWIR CLI Sensitivity**

445

446 Radioisotopes were located within either plastic Eppendorf's or glass scintillation vials and imaged  
447 with the lids off in the enclosure, whilst being held in a suitable lead pig to limit exposure. White  
448 light images were acquired with the door open and room lights on (fluorescent tube bulbs with  
449 SWIR spectral emission (Pentron 3000K, Osram Sylvania, MA, USA)).[58] Corresponding SWIR  
450 CLI was performed after closing the door and adjusting the exposure time to 10s. Black  
451 posterboard (TB5, Thorlabs, NJ, USA) was placed over the source to prevent propagation of light  
452 whilst allowing  $\gamma$  particles to pass freely.

453

### 454 **4.3 Determining the radioisotope SWIR CLI temporal resolution and emission spectrum**

455

456  $^{32}\text{P}$  ( $\beta$  energy average 0.695MeV,  $t_{1/2}$  14.3 days) was used to determine the temporal resolution  
457 limits of the setup along with the SWIR CL emission spectrum. The long half-life of the  $^{32}\text{P}$   
458 provided a constant photon flux. Approximately 10 mCi of  $^{32}\text{P}$  (NEX060005MC, Perkin Elmer, MA,  
459 USA) in 1 ml of water was imaged in the setup as previously outlined. The limit of temporal

460 acquisition was determined by acquiring 90 frames at a range of exposure times from 10 to 0.1 s.  
461 The limit of detection was defined as a level in which the source could not be visually determined  
462 from the inherent noise in the system. The SWIR CL spectrum was determined using appropriate  
463 long pass (LP) filters separated by 100 nm ranging from 1000 to 1500 nm (FELH1000:100:1500,  
464 Thorlabs, NJ, USA) mounted on the front of the lens (SM1L03 and SM1A57, Thorlabs, NJ, USA).  
465 Acquisitions were performed as outlined previously.

#### 467 **4.4 Image processing and statistical analysis**

468  
469 Image processing was carried out with the open source software Fiji (ImageJ 2.0, [59]).  
470 Processing steps are outlined in Supplementary Figure 1. Briefly, darknoise levels acquired with  
471 the same settings and conditions were subtracted from the data. Binning (8x8) was applied to  
472 improve sensitivity along with median filtering was applied to remove  $\gamma$  strikes. Artifacts were  
473 further removed via FFT transformations and ImageJ rolling ball background subtraction.[60]  
474 Finally, the image was resized for overlay with the white light image. Reported values were  
475 collected using ROI measurements in Fiji. Statistical analysis and graphing were carried out in  
476 GraphPad Prism9 (GraphPad Software LLC, CA, USA). Information on statistical analyses is  
477 given for each figure along with technical and biological replicate numbers. SWIR radiance of  
478 respective isotopes was calculated by recording gray values and correcting for isotope  
479 concentration ( $\mu\text{Ci}/\mu\text{l}$ ) and FOV ( $\text{cm}^2$ ). Full width half maximum measurements were carried out  
480 using custom code in MATLAB (2020b, Mathworks Inc., USA).

#### 481 **4.5 Silica nanoparticle radiolabeling and injection**

482  
483 Silica nanoparticles were labeled with either  $^{68}\text{Ga}$  or  $^{90}\text{Y}$  as previously described.[40] Briefly, silica  
484 nanoparticles (SiNPs) were incubated with free isotope at a pH of 8.8 for 60 mins, on a  
485 thermomixer at  $70^\circ\text{C}$  and 500 rpm. After completion of the labeling protocol, radiolabeled SiNPs  
486 were resuspended in 30  $\mu\text{l}$  of saline solution for injection into the footpad.

#### 487 **4.6 Preclinical SWIR CLI**

488  
489 All handling and mouse experiments were carried out in accordance with Institutional Animal Care  
490 and Use Committee (IACUC) guidelines at MSKCC and the NIH Guide for the Care and Use of  
491 Laboratory Animals. *In vivo* animal procedures were performed under anesthesia by inhalation of  
492 3% isoflurane in 100%  $\text{O}_2$  v/v followed by 1-2% isoflurane in 100%  $\text{O}_2$  v/v for maintenance. All  
493 mice ( $n = 13$  in total, FoxN1<sup>NU</sup>, Stock #069, Envigo, USA) were housed under appropriate  
494 conditions with food and water *ad libitum*. Anesthetized mice ( $n = 4$ ) were xenografted via injection  
495 with  $1 \times 10^6$  4T1 cells (ATCC, CRL-2539) suspended in 30  $\mu\text{l}$  of Matrigel (Corning, #354234) into  
496 the fourth mammary pad. Tumors were allowed to proliferate for 2 weeks before being imaged.  
497 In all cases mouse euthanasia was performed using  $\text{CO}_2$  in accordance with approved protocols.  
498 For Supplementary Figure 2, following euthanasia,  $n = 3$  xenografted mice were injected (blinded)  
499 with up to 4.5 mCi of  $^{18}\text{F}$ -FDG with one mouse not receiving any injection (negative control).  
500 Additionally,  $n = 1$  euthanized mouse was injected into the footpad with  $^{68}\text{Ga}$  labeled SiNPs.  
501 Finally,  $n = 4$  mice were injected with  $^{90}\text{Y}$  labeled SiNPs with an additional  $n = 1$  mouse not  
502 receiving any injection and providing a negative control for *in vivo* experiments.  
503  
504  
505

### 506 **5. Acknowledgements**

507  
508 We would like to thank Craig Wall, Manjul Shah, Sabbir Liakat and Princeton Teledyne for  
509 providing the NIRvana 640 TE camera and lens along with Photon Etc. for providing the Zephir  
510 1.7x camera. Sincere thanks go to Valerie Longo and Pat Zanzonico of the small animal imaging

511 facility at MSKCC. This work was funded by the National Institutes of Health NCI grants  
512 R01CA183953 (to Jan Grimm) and P30 CA08748 (to Craig Thompson/MSKCC).

513

## 514 **6. Conflict of Interests**

515

516 The authors declare no conflicts of interest.

517

## 518 **7. Author Contributions**

519

520 BML setup the system, designed and carried out experiments, recorded images and carried out  
521 the data analysis. QZ performed the radiolabeling of SiNPs. MS, EI, HH & AO aided *in vivo*  
522 experiments. BML, ECP & JG designed the study. All authors aided with the experimental setup,  
523 experimental procedures, data interpretation, data presentation and writing of the manuscript.

524

## 525 **References**

526

527 1. Čerenkov, P. *Visible light from pure liquids under the impact of  $\gamma$ -rays*. in *CR (Dokl.) Acad.*  
528 *Sci. URSS*. 1934.

529 2. Ciarrocchi, E. and N. Belcari, *Cerenkov luminescence imaging: physics principles and*  
530 *potential applications in biomedical sciences*. *EJNMMI physics*, 2017. **4**(1): p. 1-31.

531 3. Glaser, A.K., et al., *Cerenkov radiation fluence estimates in tissue for molecular imaging*  
532 *and therapy applications*. *Physics in Medicine & Biology*, 2015. **60**(17): p. 6701.

533 4. Ruggiero, A., et al., *Cerenkov luminescence imaging of medical isotopes*. *Journal of*  
534 *Nuclear Medicine*, 2010. **51**(7): p. 1123-1130.

535 5. Contalbrigo, M., et al., *The CLAS12 ring imaging Cerenkov detector*. *Nuclear Instruments*  
536 *and Methods in Physics Research Section A: Accelerators, Spectrometers, Detectors and*  
537 *Associated Equipment*, 2020: p. 163791.

538 6. Mitchell, G.S., et al., *In vivo Cerenkov luminescence imaging: a new tool for molecular*  
539 *imaging*. *Philosophical Transactions of the Royal Society A: Mathematical, Physical and*  
540 *Engineering Sciences*, 2011. **369**(1955): p. 4605-4619.

541 7. Tamura, R., E.C. Pratt, and J. Grimm. *Innovations in nuclear imaging instrumentation:*  
542 *Cerenkov imaging*. in *Seminars in nuclear medicine*. 2018. Elsevier.

543 8. Miao, T., et al., *Cerenkov imaging for linac beam shape analysis as a remote electronic*  
544 *quality assessment verification tool*. *Medical physics*, 2019. **46**(2): p. 811-821.

545 9. D'Souza, J.W., et al., *Cerenkov luminescence imaging as a modality to evaluate antibody-*  
546 *based PET radiotracers*. *Journal of Nuclear Medicine*, 2017. **58**(1): p. 175-180.

547 10. Olde Heuvel, J., et al., *(68)Ga-PSMA Cerenkov luminescence imaging in primary prostate*  
548 *cancer: first-in-man series*. *European journal of nuclear medicine and molecular imaging*,  
549 2020. **47**(11): p. 2624-2632.

550 11. Thorek, D.L., C.C. Riedl, and J. Grimm, *Clinical Cerenkov luminescence imaging of 18F-FDG*.  
551 *Journal of Nuclear Medicine*, 2014. **55**(1): p. 95-98.

552 12. Grootendorst, M.R., et al., *Intraoperative assessment of tumor resection margins in*  
553 *breast-conserving surgery using 18F-FDG Cerenkov luminescence imaging: a first-in-*  
554 *human feasibility study*. *Journal of Nuclear Medicine*, 2017. **58**(6): p. 891-898.

- 555 13. Jarvis, L.A., et al., *Cherenkov Video Imaging Allows for the First Visualization of Radiation*  
556 *Therapy in Real Time*. International Journal of Radiation Oncology\* Biology\* Physics, 2014.  
557 **89**(3): p. 615-622.
- 558 14. Jacques, S.L., *Optical properties of biological tissues: a review*. Physics in Medicine &  
559 Biology, 2013. **58**(11): p. R37.
- 560 15. Yaroshevsky, A., et al., *Transition from the ballistic to the diffusive regime in a turbid*  
561 *medium*. Optics letters, 2011. **36**(8): p. 1395-1397.
- 562 16. Ding, F., et al., *Recent advances in near-infrared II fluorophores for multifunctional*  
563 *biomedical imaging*. Chemical science, 2018. **9**(19): p. 4370-4380.
- 564 17. Cao, Q., et al., *Multispectral imaging in the extended near-infrared window based on*  
565 *endogenous chromophores*. Journal of biomedical optics, 2013. **18**(10): p. 101318.
- 566 18. Thorek, D.L., et al., *Quantitative imaging of disease signatures through radioactive decay*  
567 *signal conversion*. Nature medicine, 2013. **19**(10): p. 1345.
- 568 19. Zhang, Q., et al., *Ultrasmall Downconverting Nanoparticle for Enhanced Cerenkov*  
569 *Imaging*. Nano Letters, 2021. **21**(10): p. 4217-4224.
- 570 20. Pratt, E.C., et al., *Nanoparticles as multimodal photon transducers of ionizing radiation*.  
571 Nature nanotechnology, 2018. **13**(5): p. 418-426.
- 572 21. Thimsen, E., B. Sadtler, and M.Y. Berezin, *Shortwave-infrared (SWIR) emitters for*  
573 *biological imaging: a review of challenges and opportunities*. Nanophotonics, 2017. **6**(5):  
574 p. 1043-1054.
- 575 22. Carr, J.A., et al., *Shortwave infrared fluorescence imaging with the clinically approved*  
576 *near-infrared dye indocyanine green*. Proceedings of the National Academy of Sciences,  
577 2018. **115**(17): p. 4465-4470.
- 578 23. Naczynski, D.J., et al., *X-ray-induced shortwave infrared biomedical imaging using rare-*  
579 *earth nanoprobes*. Nano letters, 2015. **15**(1): p. 96-102.
- 580 24. Cao, X., et al., *Cherenkov excited short-wavelength infrared fluorescence imaging in vivo*  
581 *with external beam radiation*. Journal of biomedical optics, 2018. **24**(5): p. 051405.
- 582 25. Dothager, R.S., et al., *Cerenkov radiation energy transfer (CRET) imaging: a novel method*  
583 *for optical imaging of PET isotopes in biological systems*. PloS one, 2010. **5**(10): p. e13300.
- 584 26. Cao, X., et al., *Observation of short wavelength infrared (SWIR) Cherenkov emission*.  
585 Optics letters, 2018. **43**(16): p. 3854-3857.
- 586 27. Glaser, A.K., et al., *Optical dosimetry of radiotherapy beams using Cherenkov radiation:*  
587 *the relationship between light emission and dose*. Physics in Medicine & Biology, 2014.  
588 **59**(14): p. 3789.
- 589 28. Glaser, A.K., et al., *Time-gated Cherenkov emission spectroscopy from linear accelerator*  
590 *irradiation of tissue phantoms*. Optics Letters, 2012. **37**(7): p. 1193-1195.
- 591 29. Browne, E., *Commonly used radioactive sources*. The European Physical Journal. C,  
592 Particles and Fields., 2000. **15**(1-4): p. 190-190.
- 593 30. Pritychenko, B., et al., *The nuclear science references (NSR) database and web retrieval*  
594 *system*. Nuclear Instruments and Methods in Physics Research Section A: Accelerators,  
595 Spectrometers, Detectors and Associated Equipment, 2011. **640**(1): p. 213-218.
- 596 31. Tendler, I.I., et al., *Experimentally observed cherenkov light generation in the eye during*  
597 *radiation therapy*. International Journal of Radiation Oncology\* Biology\* Physics, 2020.  
598 **106**(2): p. 422-429.

- 599 32. Darr, C., et al., *Intraoperative 68Ga-PSMA Cerenkov luminescence imaging for surgical*  
600 *margins in radical prostatectomy: a feasibility study*. Journal of Nuclear Medicine, 2020.  
601 **61**(10): p. 1500-1506.
- 602 33. Banerjee, S.R. and M.G. Pomper, *Clinical applications of Gallium-68*. Applied Radiation  
603 and Isotopes, 2013. **76**: p. 2-13.
- 604 34. Beattie, B.J., et al., *Quantitative modeling of Cerenkov light production efficiency from*  
605 *medical radionuclides*. PloS one, 2012. **7**(2): p. e31402.
- 606 35. Martin, T. and P. Dixon, *InGaAs sees infrared and visible light*. Laser focus world, 2004.  
607 **40**(11): p. 109-111.
- 608 36. Williamson, J.B., et al., *High-density, planar Zn-diffused InGaAs/InP photodetector arrays*  
609 *with extended short-wavelength response*. IEEE Transactions on Electron Devices, 1991.  
610 **38**(12): p. 2707.
- 611 37. Hoelter, T.R. and J.B. Barton. *Extended short-wavelength spectral response from InGaAs*  
612 *focal plane arrays*. in *Infrared Technology and Applications XXIX*. 2003. International  
613 Society for Optics and Photonics.
- 614 38. Kim, S.P., et al., *A guide to 90Y radioembolization and its dosimetry*. Physica Medica, 2019.  
615 **68**: p. 132-145.
- 616 39. Fidelman, N., et al., *Radioembolization with 90Y glass microspheres for the treatment of*  
617 *unresectable metastatic liver disease from chemotherapy-refractory gastrointestinal*  
618 *cancers: final report of a prospective pilot study*. Journal of gastrointestinal oncology,  
619 2016. **7**(6): p. 860.
- 620 40. Shaffer, T.M., et al., *Silica nanoparticles as substrates for chelator-free labeling of*  
621 *oxophilic radioisotopes*. Nano letters, 2015. **15**(2): p. 864-868.
- 622 41. Demirci, E., et al., *Estimation of the organ absorbed doses and effective dose from 68Ga-*  
623 *PSMA-11 PET scan*. Radiation protection dosimetry, 2018. **182**(4): p. 518-524.
- 624 42. Carpenter, C.M., et al., *Cerenkov luminescence endoscopy: improved molecular sensitivity*  
625 *with  $\beta$ -emitting radiotracers*. Journal of Nuclear Medicine, 2014. **55**(11): p. 1905-1909.
- 626 43. Alsheikh, H., *[P091] Investigation of cherenkov imaging using IVIS bioluminescence*  
627 *scanner*. Physica Medica: European Journal of Medical Physics, 2018. **52**: p. 127.
- 628 44. Spinelli, A.E., et al., *Multispectral Cerenkov luminescence tomography for small animal*  
629 *optical imaging*. Optics Express, 2011. **19**(13): p. 12605-12618.
- 630 45. de Wit-van der Veen, B., et al., *Performance evaluation of Cerenkov luminescence*  
631 *imaging: a comparison of 68Ga with 18F*. EJNMMI physics, 2019. **6**(1): p. 1-13.
- 632 46. Carr, J.A., et al., *Absorption by water increases fluorescence image contrast of biological*  
633 *tissue in the shortwave infrared*. Proceedings of the National Academy of Sciences, 2018.  
634 **115**(37): p. 9080-9085.
- 635 47. Zhang, H., et al., *Penetration depth of photons in biological tissues from hyperspectral*  
636 *imaging in shortwave infrared in transmission and reflection geometries*. Journal of  
637 biomedical optics, 2016. **21**(12): p. 126006.
- 638 48. Balkin, E.R., et al., *In vivo localization of 90Y and 177Lu radioimmunoconjugates using*  
639 *Cerenkov luminescence imaging in a disseminated murine leukemia model*. Cancer  
640 research, 2014. **74**(20): p. 5846-5854.

- 641 49. Liu, M., et al., *Cerenkov luminescence imaging on evaluation of early response to*  
642 *chemotherapy of drug-resistant gastric cancer*. *Nanomedicine: Nanotechnology, Biology*  
643 *and Medicine*, 2018. **14**(1): p. 205-213.
- 644 50. Zhang, Z., et al., *Endoscopic Cerenkov luminescence imaging and image-guided tumor*  
645 *resection on hepatocellular carcinoma-bearing mouse models*. *Nanomedicine:*  
646 *Nanotechnology, Biology and Medicine*, 2019. **17**: p. 62-70.
- 647 51. Zhao, S., et al., *Cerenkov luminescence imaging is an effective preclinical tool for assessing*  
648 *colorectal cancer PD-L1 levels in vivo*. 2020.
- 649 52. Fraenkel, R., et al. *Development of low-SWaP and low-noise InGaAs detectors*. in *Infrared*  
650 *Technology and Applications XLIII*. 2017. International Society for Optics and Photonics.
- 651 53. Hu, Z., et al., *Construction of a Novel Intraoperative Cerenkov luminescence Imaging*  
652 *System for Image-Guided Resection of Colorectal Cancer on Patients*. *Journal of Nuclear*  
653 *Medicine*, 2017. **58**(supplement 1): p. 527-527.
- 654 54. Grootendorst, M. and A. Purushotham, *Clinical feasibility of intraoperative 18F-FDG*  
655 *Cerenkov Luminescence Imaging in breast cancer surgery*. *Journal of Nuclear Medicine*,  
656 2015. **56**(supplement 3): p. 13-13.
- 657 55. Zhang, Z., et al., *A novel in vivo Cerenkov luminescence image-guided surgery on primary*  
658 *and metastatic colorectal cancer*. *Journal of biophotonics*, 2020. **13**(3): p. e201960152.
- 659 56. Xu, Y., et al., *Proof-of-concept study of monitoring cancer drug therapy with Cerenkov*  
660 *luminescence imaging*. *Journal of Nuclear Medicine*, 2012. **53**(2): p. 312-317.
- 661 57. Huang, Y.-H., et al., *10-Gb/s InGaAs pin photodiodes with wide spectral range and*  
662 *enhanced visible spectral response*. *IEEE Photonics Technology Letters*, 2007. **19**(5): p.  
663 339-341.
- 664 58. Elvidge, C.D., et al., *Spectral identification of lighting type and character*. *Sensors*, 2010.  
665 **10**(4): p. 3961-3988.
- 666 59. Schindelin, J., et al., *Fiji: an open-source platform for biological-image analysis*. *Nature*  
667 *methods*, 2012. **9**(7): p. 676-682.
- 668 60. Walter, J., *FFT-filter*. Available at: <http://rsb.info.nih.gov/ij/plugins/fft-filter.html>., 2001.  
669

## Supplementary Files

This is a list of supplementary files associated with this preprint. Click to download.

- [SWIRCLISUPP21.pdf](#)